size and wall thickness and would emerge from the heart in close proximity to the identified arch. It is not possible to deduce the embryologic origin of the single aorta, to verify whether its development paralleled that of birds or mammals (*13, 14*). The radiographic topology of the aorta is essentially identical in adults of both groups (*15*). The estimated weight of the heart, based on axial and transverse measurements, a 20% compression effect on a conic volume, and a tissue density of 1 gm/cm^3, ranges between 1.6 and 1.9 kg, which is quite consistent with predictions (1.5 to 1.8 kg) from regressions based on body weight (*16*). We do not possess evidence that would allow us to reliably identify other structures within the pericardial region. However, the preservation of heartlike structures within an uncrushed thoracic cavity of one small dinosaur suggests that well-preserved vertebrate skeletons should routinely be examined for traces of non-osseous tissues.

In general terms, dinosaurs appear to have been morphologically intermediate between modern crocodiles and birds. This has led to the inference that the heart of ancestral dinosaurs might have resembled that of crocodiles (*1*), in which left and right systemic aortas are present and are linked by a foramen of Panizza. This foramen can allow either right-to-left or left-to-right shunting of blood, depending on the phase of the cardiac cycle and a variety of physiological variables, including the activity level of the animal, that affect heart contractility and vascular resistance (*17*). Reid (*1*) has suggested that in dinosaurs the foramen of Panizza was closed, and the blood from the left ventricle flowed into a single (right) systemic aorta, as in birds. The basis for his speculation is the need to generate pressure sufficient to circulate blood throughout the body of a large erect animal. We suggest that the primary advantage of this adaptation was to improve systemic oxygenation, thereby supporting higher metabolic rates. It is hypothesized that physiologically controlled right-to-left shunting confers advantages on animals with low metabolic rates by, among other things, reducing cardiac energy requirements (*18*), although this has recently been questioned (*17*). In birds and mammals, shunting is clearly detrimental. It diminishes an animal's tolerance for sustained exercise by reducing the efficiency of systemic oxygen delivery to tissues with a generally much higher oxygen demand than those of living ectotherms. A four-chambered cardiovascular system with a single systemic aorta communicating with the left ventricle greatly reduces the risk of shunting and can be considered a means of more efficiently supporting prolonged periods of high activity.

Of the many clades of dinosaurs (*4*), in at least one (hypsilophodontids) there is now evidence of an advanced heart with a single systemic aorta. Because of the presence of similar hearts in birds, which are generally considered to be theropod derivatives (*3, 4*), it might be concluded that ancestral dinosaurs also possessed an advanced heart (thus making the attribute a synapomorphy for dinosaurs). However, in view of the enormous span of time (>150 million years) separating ancestral dinosaurs from the specimen under consideration (*4*), we are uncertain that the effects of long-term parallel selection and evolution on the cardiovascular system were negligible. Whether high metabolic rates and advanced hearts arose once or more than once among dinosaurs remains an open question.

References and Notes

1. R. E. H. Reid, in *The Complete Dinosaur*, J. O. Farlow and M. K. Brett-Surman, Eds. (Indiana Univ. Press, Bloomington, IN, 1997), pp. 449–473.
2. J. O. Farlow, in *The Dinosauria*, D. B. Weishampel, P. Dodson, H. Osmolska, Eds. (Univ. of California Press, Berkeley, CA, 1990), pp. 43–55.
3. K. Padian, *Nature* **393**, 729 (1998).
4. P. C. Sereno, *Science* **284**, 2137 (1999).
5. R. E. Barrick, M. K. Stoskopf, W. J. Showers, in *The Complete Dinosaur*, J. O. Farlow and M. K. Brett-Surman, Eds. (Indiana Univ. Press, Bloomington, IN, 1997), pp. 474–490.
6. C. W. Gilmore, *Proc. U.S. Natl. Mus.* **49**, 501 (1915).
7. P. M. Galton, *Rev. Paleobiol.* **16**, 231 (1997).
8. J. F. Anderson, A. Hall-Martin, D. A. Russell, *J. Zool. (London)* **207**, 53 (1985).
9. G. S. Paul, in *Dinofest International: A Symposium Sponsored by Arizona State University*, D. L. Wolberg, E. Stump, G. Rosenberg, Eds. (Academy of Natural Sciences, Philadelphia, 1997), pp. 129–154.
10. C. Dal Sasso and M. Signore, *Nature* **392**, 383 (1998); J. A. Ruben *et al.*, *Science* **283**, 514 (1999).
11. M. J. Benton, *Trends Ecol. Evol.* **13**, 303 (1998).
12. J. Weigelt, *Recent Vertebrate Carcasses and Their Paleobiological Implications* (Univ. of Chicago Press, Chicago, 1989).
13. H. Butler and B. H. J. Juurlink, *An Atlas for Staging Mammalian and Chick Embryos* (CRC Press, Boca Raton, FL, 1987).
14. A. Feduccia and E. McCrady, *Torrey's Morphogenesis of the Vertebrates* (Wiley, New York, ed. 5, 1991).
15. D. E. Thrall, *Textbook of Veterinary Diagnostic Radiology* (Saunders, Philadelphia, ed. 3, 1998).
16. F.V. Paladino, J. R. Spotila, P. Dodson, in *The Complete Dinosaur*, J. O. Farlow and M. K. Brett-Surman, Eds. (Indiana Univ. Press, Bloomington, IN, 1977), pp. 491–504.
17. J. W. Hicks, in *Reptiles: Mechanisms, Regulation and Physiological Function*, vol. 19 of *Biology of the Reptilia*, C. Gans and A. S. Gaunt, Eds. (Society for the Study of Amphibians and Reptiles, Ithaca, NY, 1998), pp. 425–483.
18. W. W. Burggren and S. J. Warburton, *Cardioscience* **5**, 183 (1994).

19. The authors are grateful to B. Bennett and V. Schneider of the North Carolina State Museum of Natural Sciences for access to the specimen, to W. H. Straight for XRD analyses, and to R. Lea for his advice and encouragement. A.K. thanks D. Perry for the CT scans; the Ashland Community and Rogue Valley hospitals for access to CT equipment; and cardiologists of Cardiology Consultants PC of Medford, OR, for their comments on the possible fossil cardiac structures. T. Jetton assisted M.H. in the preparation of the dinosaur specimen.

9 March 2000; accepted 27 March 2000

A Structural Framework for Deciphering the Link Between I-A^{g7} and Autoimmune Diabetes

Adam L. Corper,[1]* Thomas Stratmann,[2]* Vasso Apostolopoulos,[1] Christopher A. Scott,[1]† K. Christopher Garcia,[1]‡ Angray S. Kang,[1]§ Ian A. Wilson,[1]‖ Luc Teyton[2]‖

Susceptibility to murine and human insulin-dependent diabetes mellitus correlates strongly with major histocompatibility complex (MHC) class II I-A or HLA-DQ alleles that lack an aspartic acid at position β57. I-A^{g7} lacks this aspartate and is the only class II allele expressed by the nonobese diabetic mouse. The crystal structure of I-A^{g7} was determined at 2.6 angstrom resolution as a complex with a high-affinity peptide from the autoantigen glutamic acid decarboxylase (GAD) 65. I-A^{g7} has a substantially wider peptide-binding groove around β57, which accounts for distinct peptide preferences compared with other MHC class II alleles. Loss of Asp$^{\beta 57}$ leads to an oxyanion hole in I-A^{g7} that can be filled by peptide carboxyl residues or, perhaps, through interaction with the T cell receptor.

MHC genes have been linked with susceptibility in almost all autoimmune diseases (*1*). In the case of insulin-dependent diabetes mellitus (IDDM), a role for particular murine I-A alleles and their human homologs, HLA-DQ, has been inferred from numerous studies. Sequence analysis of these alleles has highlighted the importance of a key residue, β57; an Asp at position 57 of the class II β-chain is correlated with IDDM resistance, while neutral residues Ser, Ala, or Val are linked to disease susceptibility (*2, 3*).

The nonobese diabetic (NOD) mouse provides a model system for the study of IDDM. I-A^{g7} is the only MHC class II molecule expressed in NOD mice and is strongly linked to disease susceptibility. I-A^{g7} shares the same α chain as the non–IDDM-linked

allele I-A^d (*4*), but contains a unique β chain that differs by 17 residues (*2*) and, hence, defines the diabetogenic characteristics of I-A^{g7}. Two polymorphic residues, $His^{\beta 56}$ and $Ser^{\beta 57}$, play a pivotal role in linking I-A^{g7} with IDDM; reintroduction by trangenesis of either $Pro^{\beta 56}$ (*5*) or $Asp^{\beta 57}$ (*6*) into I-A^{g7} reduces markedly the incidence of diabetes in NOD mice. The effector mechanisms linking variation at position β57 with IDDM susceptibility remain unclear; however, acquisition of an acidic residue at position 9 (P9) in the bound peptide may compensate for the lost charge on the class II molecule (*7*, *8*). On the other hand, most I-A/HLA-DQ molecules do not display a clear peptide-binding motif, such as described for MHC class I and for other class II I-E/HLA-DR molecules, suggesting greater promiscuity in peptide binding (*7*).

Several hypotheses suggest that I-A^{g7} could bear unusual structural features that could translate at the T cell level into high autoreactivity, poor thymic tolerance, and inefficacious peripheral tolerance (*9*, *10*). Alternatively, I-A^{g7} may bind and present a unique set of peptides that are not usually presented by other MHC haplotypes (*11*).

We explored the structural link between I-A^{g7} and autoimmunity by expressing I-A^{g7} and I-A^d in *Drosophila melanogaster* cells as "functionally" empty molecules and as peptide-MHC (pMHC) complexes. Empty molecules were used for peptide-binding studies with synthetic peptides and phage-displayed peptide libraries, while single pMHC complexes were crystallized for x-ray structure analysis. Both MHC molecules were expressed by attaching complementary acidic and basic leucine zippers to the α- and the β-chain COOH-termini (*12*). A single pMHC was expressed by covalently tethering the peptide sequence to the NH_2-terminus of the β chain, as described (*12*, *13*). Removal of the leucine zipper by thrombin digestion did not destabilize the I-A^{g7} dimer, as tested by gel filtration (*14*). The recombinant soluble I-A^d and I-A^{g7} molecules did not exhibit a tendency to aggregate or to bind peptides poorly; however, both were similarly SDS-unstable.

Our previously determined crystal structure of I-A^d with two different peptides (*15*) showed that relatively small hydrophobic side chains were generally used to insert into the P4, P6, and P9 pockets. We have confirmed the absence of a highly restricted motif for I-A^d by selecting a 12–amino acid random peptide phage library against empty I-A^d (*16*). The selection (panning) of the same library against empty I-A^{g7} again did not reveal an obvious binding motif, but resulted in an increase in the frequency of acidic residues (Glu and Asp) within the last four residues of the peptide compared with the naïve and the I-A^d–selected library. Binding of an 11–amino acid polyalanine peptide to both I-A^d and I-A^{g7} (*17*) confirmed promiscuity in peptide binding, as this peptide displayed median inhibitory concentrations (IC_{50}'s) of 1.5 and 0.11 μM, respectively (Fig. 1A). However, substitution of Ala^{P9} by Glu^{P9} resulted in a loss of binding for I-A^d, but a 10-fold increase for I-A^{g7} (Fig. 1A). A nested series of 15–amino acid peptides (overlapping by three residues), encompassing all but the last six residues of GAD65, showed that of the 48 peptides, only one was a strong I-A^d binder [four others were medium binders (Fig. 1B)], whereas for I-A^{g7}, there were five strong, five medium, and three poor binders (Fig. 1B). These peptide data suggest increased promiscuity of I-A^{g7} relative to I-A^d.

To identify self peptides for I-A^{g7}, we constructed a 45- to 75-nucleotide random gene fragment phage display library from the cDNA of murine GAD65, an autoantigen that has been implicated in the early pathogenesis of diabetes (*18*). Selection of the library against empty I-A^{g7} resulted in the multiple identification of two main GAD sequences, residues 207 to 217 and 105 to 119. $GAD_{206\text{-}220}$ represents one of the major epitopes recognized by NOD mice, in vivo, after GAD65 immunization (*19*, *20*). Both peptides bound strongly to I-A^{g7} in an in vitro binding assay, with $GAD_{207\text{-}220}$ (YEIAPVFV-LLEYVT) being the better binder (IC_{50} = 0.08 μM). Binding of $GAD_{207\text{-}220}$ by I-A^{g7} was entirely lost when Glu_{217} (equivalent to P9) was replaced by glutamine.

The crystal structure of I-A^{g7} covalently linked to residues 207 to 220 of murine GAD65 was determined at 2.6 Å resolution

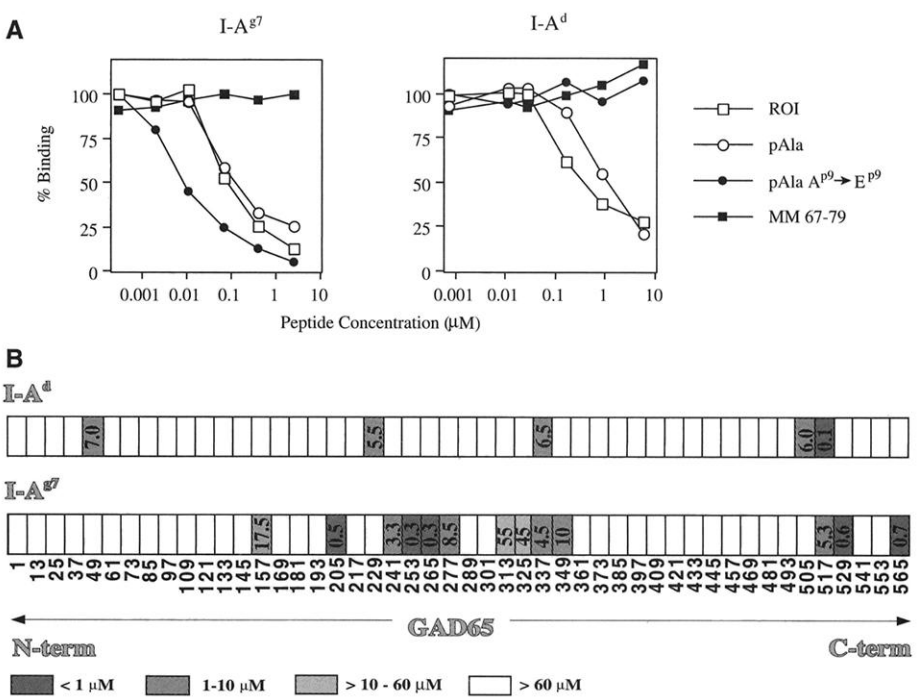

Fig. 1. Comparison of peptide binding to I-A^d and I-A^{g7}. (**A**) Percentage of binding of biotinylated ROI peptide in the presence of increasing concentrations of test peptide (*17*). An 11–amino acid polyalanine (pAla) peptide binds to both MHC molecules in a similar manner to ROI. Substitution of Ala^{P9} by Glu (pAla A^{P9} →E) increases binding to I-A^{g7}, but abolishes binding to I-A^d. Both alleles bind to the positive control peptide ROI but not to MM67–79 (negative control). (**B**) At the level of a single protein, such as GAD65, I-A^{g7} binds more peptide fragments than I-A^d. The binding of I-A^{g7} and I-A^d, to a collection of 48 15–amino acid peptides encompassing all but the last six residues of GAD65, was tested by using an inhibition assay (*17*). The schematic indicates the approximate IC_{50} of peptide binding for each nested peptide and is based on an average of two independent experiments. The IC_{50} of the control peptide, ROI, is 0.5 μM. Peptides used for this analysis were synthesized in a 96-well format with FMOC (9-fluorenyl methoxycarbonyl) chemistry with a multiple pin synthesizer (Chiron Technologies, San Diego, CA). The purity of peptides exceeded 80%. The starting position of each 15–amino acid peptide, relative to GAD65, is displayed underneath each block.

[1]Department of Molecular Biology and Skaggs Institute for Chemical Biology, [2]Department of Immunology, The Scripps Research Institute, 10550 North Torrey Pines Road, La Jolla, CA 92037, USA.

*These authors contributed equally to this work.
†Present address: Department of Medicine 0613-C, University of California, San Diego, 9500 Gilman Drive, La Jolla, CA 92083–0613, USA.
‡Present address: Stanford University School of Medicine, Departments of Microbiology and Immunology and Structural Biology, Fairchild Sciences Building D-319, 299 Campus Drive, Stanford, CA 94305, USA.
§Present address: Abgenix Inc., 7601 Dumbarton Circle, Fremont, CA 94555, USA.
‖To whom correspondence should be addressed. E-mail: wilson@scripps.edu; lteyton@scripps.edu

(Table 1). The electron density identified residues 209 to 217 as the P1 to P9 core of the bound peptide (Table 1 and Fig. 2A); all 14 residues of the GAD peptide had interpretable main-chain density and occupied the P−2 to P12 register [Web table 1 (*21*)]. The P1, P4, and P6 pockets contained the hydrophobic residues Ile-209, Val-212, and Val-214, respectively, whereas the P9 pocket was occupied by Glu-217. A C_α superimposition (*22*) of I-A^{g7} onto I-A^d (*15*, *23*) and I-A^k (*24*) gave low root mean square (rms) deviations of 0.26 and 0.31 Å, respectively, as expected from their high sequence identity. The antiparallel β sheet that forms the floor of the peptide groove and the long α helix of the α_1 domain overlayed well in all three structures (Fig. 2B). However, the α-helical segments of the β_1 domain diverged progressively from the H2b to the H2a and H1 helical segments; the H1 segment containing residue β57 of the I-A^{g7} helix exhibited a noticeable displacement away from the binding groove (*25*) that was partly caused by the polymorphic residues $His^{\beta 9}$ and $Tyr^{\beta 61}$ (Fig. 2, B and C). $Tyr^{\beta 61}$ appears to play the major role here as it is unique to I-A^{g7} (Trp in I-A^d and I-A^k), whereas $His^{\beta 9}$ is also found in I-A^k [Val in I-A^d (*26*)].

Most murine and human MHC II molecules contain a highly conserved interdomain salt bridge between residues $Arg^{\alpha 76}$ and $Asp^{\beta 57}$. Absence of this salt bridge in I-A^{g7}, owing to the presence of $Ser^{\beta 57}$, has been proposed to cause interdomain instability and loose fitting of the peptide COOH-terminus (*27*). Our results do not support this view, because the COOH-terminal residues of the peptide are well defined in the electron density until P12 (*28*). There is some rearrangement of the hydrogen-bonding network, involving COOH-terminal peptide residues P7 to P9, as a result of MHC polymorphic differences in this region; however, the total number of main-chain hydrogen bonds remains unchanged compared with I-A^d [Fig. 3, A to D (*29*)].

The absence of the salt bridge between residues $Arg^{\alpha 76}$ and $Ser^{\beta 57}$ does not in itself significantly alter the location of the $Arg^{\alpha 76}$ side chain (Fig. 2C). However, the $Arg^{\alpha 76}$ side chain shifts slightly to optimize hydrogen bonds with the carbonyl oxygen of $Leu^{\beta 53}$ and the side-chain hydroxyl of $Ser^{\beta 57}$. Additional compensation for the lost $Arg^{\alpha 76}$-$Asp^{\beta 57}$ salt bridge is provided by formation of a new electrostatic interaction between the P9 carboxyl of Glu-217 and $Arg^{\alpha 76}$ (*30*). The Glu-217 carboxyl also forms a hydrogen bond with the substituted $Ser^{\beta 57}$ [Web table 1 (*21*)]. Thus, Glu-217 appears to accomplish two roles: (i) It complements the charge of $Arg^{\alpha 76}$, and (ii) owing to movement of the β_1-chain H1 helix, it fills a new cavity that arises between I-A^{g7} and the peptide as a result of the substitutions at β56 and β57 (Fig. 3A).

The displacement of residue β57 away from the peptide-binding groove results in a shallow P9 pocket that is substantially wider than deep and allows the P9 side chain to have a greater degree of lateral freedom than in other class II molecules (Fig. 2D). Thus, two orientations are

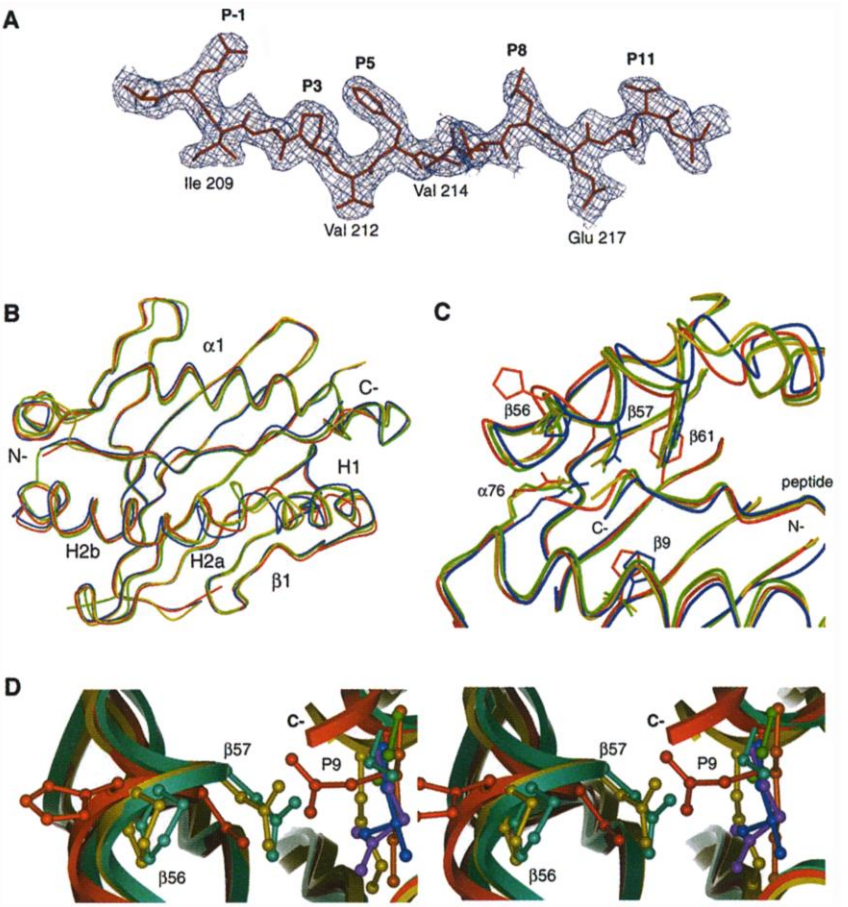

Fig. 2. Structure analysis of I-A^{g7}–$GAD_{207\text{-}220}$ and comparison with other murine MHC class II alleles. (**A**) Cross-validated σ_A-weighted $2F_o - F_c$ electron density of the $GAD_{207\text{-}220}$ peptide. The map, contoured at 1σ, represents the final refined structure. Electron density for the peptide main-chain atoms is present for residues P−2 to P12; however, convincing side-chain density for Tyr-207 (P−2), Tyr-218 (P10), and Thr-220 (P12) was absent (*59*). The side chains for these residues were therefore truncated back to C_β. Final coordinates are overlaid in the map. (**B**) Overlay of the murine MHC class II molecules I-A^{g7} (red), I-A^d (yellow, green), and I-A^k (blue). The C_α trace (*22*) shows only the α_1 and β_1 domain of the respective MHC II molecule. The two I-A^d pMHC complexes are colored green (peptide $OVA_{323\text{-}339}$; PDB code 1IAO) and yellow (peptide $HA_{126\text{-}138}$; PDB code 2IAD), respectively. The peptide COOH- and NH_2-termini are respectively labeled N- and C-. The peptide core (P1 to P9) overlays well in all four structures. (**C**) Key residues that differ in I-A^{g7} around the P9 pocket, their effect on peptide presentation, and the position of H1 and H2a segments of the β_1-chain α helices. The polymorphic residues $His^{\beta 56}$, $Ser^{\beta 57}$, and $Tyr^{\beta 61}$ (H1) are found in I-A^{g7}, but not in other I-A alleles. The presence of $Ser^{\beta 57}$, in place of the highly conserved $Asp^{\beta 57}$, substantially alters the specificity of the P9 pocket. The orientation of the $Tyr^{\beta 61}$ side chain plays a significant role in the displacement of the H1 helical segment; the side-chain phenyl ring is almost perpendicular to that observed for the indole of the corresponding Trp residue in I-$A^{d,k}$. Displacement of the β_1 H1 helical segment allows the side chain of $Tyr^{\beta 61}$ to be accommodated and dramatically alters the shape of the P9 pocket. (**D**) Unique character of the I-A^{g7} P9 pocket. The presence of $Ser^{\beta 57}$ in I-A^{g7}, coupled with displacement of the H1 helix away from the peptide groove, increases the lateral freedom for the P9 peptide side chain, as clearly seen from a comparison of I-A^{g7} (red) with I-A^d (cyan), I-A^k (green), I-E^k (gold), HLA-DR1 (purple and blue), and HLA-DR3 (yellow). The P9 side chains for all except I-A^{g7} point downward in a classical manner. Three other MHC class II molecules are not shown: HLA-DR1 [PDB code 1SEB (*60*)] was built with a polyalanine peptide. HLA-DR2 is unusual in that the P9 side chain points toward the side of the peptide groove rather than downward in the classical manner. This orientation occurs as a result of an elevated COOH-terminus of the peptide and suboptimal occupancy of the P9 pocket, because the pocket itself is identical to that found in HLA-DR1 (*61*). HLA-DR4 [PDB code 2SEB (*62*)] has a glycine at P9. Stereo versions of Fig. 2, B and C, are available from *Science* Online as Web figure 1 (*21*).

possible for the P9 side chain in I-A^{g7}; one points downward into the peptide groove and the other points sideways. The shallowness of the P9 pocket suggests that only small side chains (Gly, Ala, and possibly Ser) can be accommodated in a downward orientation. The unique sideways orientation (Fig. 2D) could accommodate medium to large side chains, although the positively charged environment would favor negatively charged residues. Modeling of a Glu at P9 into either I-A^{d}, I-A^{k}, or I-E^{k} (with the GAD$_{207–220}$ peptide) (Fig. 3, B to D, right panels) shows that, in contrast to I-A^{g7}, an acidic residue would be strongly disfavored because of a combination of poor steric and poor electrostatic complementarity.

The class II–associated invariant chain CLIP peptide dissociates rapidly from I-A^{g7} primarily because of a poor fit of Met P9; substitution by an Asp greatly enhanced the stability of this complex (*31*). The I-A^{g7} crystal structure suggests that the side chain of Met would have to point sideways, but it would not be favored in the polar P9 side pocket. For I-A^{g7} peptides that do not have a negatively charged residue at P9, a nearby negatively charged residue, such as at P11, might substitute. Modeling of a peptide with a P11 Glu (or Asp) shows that the side chain could be positioned to provide electrostatic complementarity with Arg$^{\alpha 76}$ after some main-chain rearrangements to P10 and P11.

His$^{\beta 56}$, the other key polymorphic residue, is positioned adjacent to the peptide groove and does not interact with the peptide directly. Its presence (and to a lesser extent that of Ser$^{\beta 57}$) leads to a significant increase (~44%) in the exposed molecular surface area of the Arg$^{\alpha 76}$ side chain relative to I-A^{d}, I-A^{k}, and I-E^{k} [Fig. 2C (*32*)]; thus, these two substitutions in I-A^{g7} make the P9 cavity more accessible and at the same time more attractive to oxyanions, such as carboxylates [Fig. 3, A to D (*33*)].

The I-A^{g7} pockets P1, P4, and P6 are approximately the same size as those found in

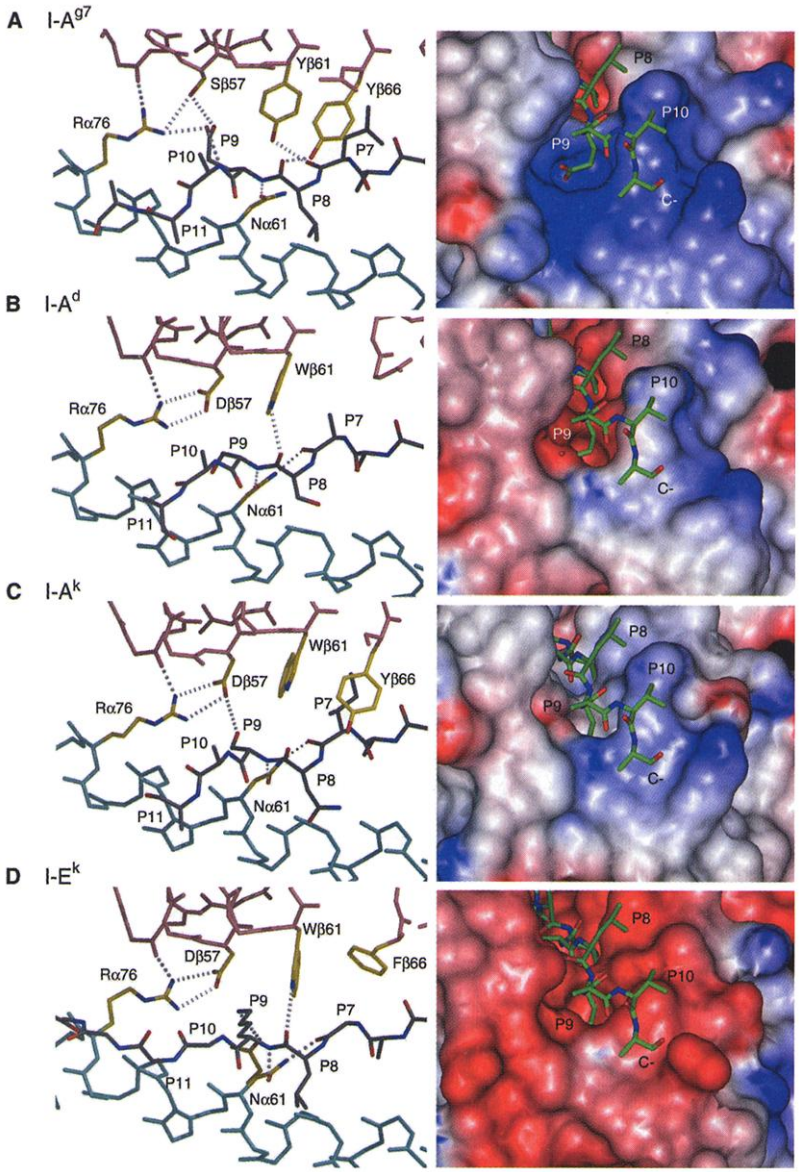

Fig. 3. (**A** to **D**) Composite highlighting the differences between I-A^{g7} and other murine class II alleles. (Left) Changes in hydrogen bonding between I-A^{g7} and the peptide P7 to P9 positions compared with other alleles. Hydrogen bonds (dotted) were calculated with HBPLUS (*63*). In I-A^{g7}, the presence of the polymorphic residues Ser$^{\beta 57}$, Tyr$^{\beta 61}$, and Tyr$^{\beta 66}$ results in a substantial alteration of the hydrogen bonding pattern to the peptide. Hydrogen bonds mediated by solvent are not shown. The backbone of the β chain is colored pink, the α chain is cyan, and the peptide is dark blue. The MHC side chains are colored yellow-green with oxygens in red and nitrogens in blue. (Right) Altered surface shape and electrostatics of the I-A^{g7} binding groove compared with other murine class II alleles. Molecular surfaces were calculated with a probe radius of 1.4 Å (*64*). Only the surface around the P9 pocket is shown. Electrostatics were calculated with the Delphi module within Insight II (*41*). Formal charges were assigned to the protein coordinates. Positive charge is contoured blue, while negative charge is red (−5 to +5 kT/e). For each allele, the GAD$_{207}$ peptide (green) is overlaid in each to allow an equivalent spatial comparison. The "carboxyl" cavity, occupied by the side chain of Glu-217, next to the P9 pocket of I-A^{g7} is readily apparent; this oxyanion hole is absent in the other I-A and I-E alleles, as evidenced by the buried terminus of Glu-217. The P9 pocket of I-A^{g7} is clearly positively charged unlike the other alleles, which range from neutral to strongly negative. Stereo versions of both panels are available from *Science* Online as Web figures 2 and 3 (*21*).

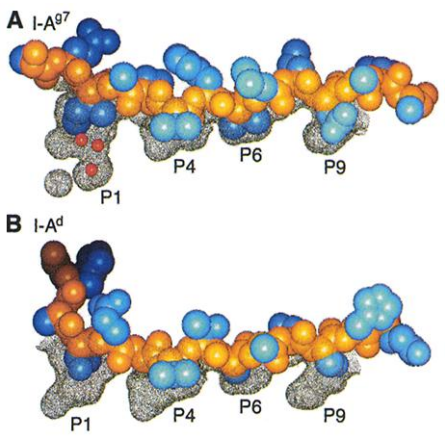

Fig. 4. Comparison of the peptide specificity pockets of (**A**) I-A^{g7} and (**B**) I-A^{d} . Molecular surfaces were calculated with a probe radius of 1.4 Å (*64*). The peptides are in spacefilling (CPK) representation (backbone, yellow; side chain, dark blue). Waters, rendered as spheres of one-half van der Waals (VDW) radii, are colored red. The P1, P4, and P6 pockets of I-A^{g7} and I-A^{d} (*15*) are about the same size, whereas the P9 pocket of I-A^{d} is larger but lacks the additional side cavity. I-A^{g7} appears to maintain some conformational flexibility in defining the shape of the P1 pocket; repositioning of Leu$^{\alpha 31}$ and Trp$^{\alpha 43}$, compared with the analogous residues in I-A^{d}, allows the P1 pocket to be occupied by the Ile-209 side chain (and three water molecules).

I-A^d [Fig. 4, A and B (*15*)]. The P1 pocket of I-A^{g7} is the largest and is only partially occupied by an Ile and three buried water molecules (Fig. 4A). The surface of the P1 pocket is formed by hydrophilic residues His$^{\alpha 24}$, Asn$^{\beta 82}$, Thr$^{\beta 86}$, and Glu$^{\beta 87}$ and hydrophobic residues Tyr$^{\alpha 8}$, Leu$^{\alpha 31}$, Phe$^{\alpha 32}$, Trp$^{\alpha 43}$, Ile$^{\alpha 52}$, and Phe$^{\alpha 54}$. This diverse set of residues could permit a broad specificity in the type and size of the P1 residue. The P4 pocket is small, hydrophobic in character, and only partially occupied by a Val; the additional space could accommodate larger hydrophobic residues, such as leucine or isoleucine. The P6 pocket, although formed mainly by hydrophobic residues, does have some polar character due to Glu$^{\alpha 66}$ and the backbone carbonyl of Asn$^{\alpha 62}$. This dual character could allow both small hydrophobic or small hydrophilic residues. Thus, on the basis of peptide-binding studies and the crystal structure, we propose the following optimal peptide-binding motif for I-A^{g7}: P1, degenerate; P4, small to medium hydrophobic residue; P6, small to medium hydrophobic or hydrophilic residue; and P9, negatively charged residue or Gly, Ala, or Ser.

Most of the higher affinity peptides that bind to I-A^{g7} can be aligned with this motif (Table 2). The CLIP$_{86\text{-}100}$ and GAD$_{105\text{-}119}$ sequences were fitted by allowing a nonoptimal residue at P9. The inability to align a few peptides, such as human GAD$_{247\text{-}266}$ (*34*), with this motif is to be expected given its relatively low stringency. Our analysis of I-A^{g7}–binding peptides from the GAD65 15–amino acid library further supports this structural motif, with only a few exceptions. Of the 13 peptides that bound to I-A^{g7}, 8 could clearly be aligned; a further 3 required a Phe or Tyr to be positioned in either P4 or P6. Also, the average IC$_{50}$ of the peptides with a negatively charged residue at P9 is indeed lower (i.e., three good binders and one medium binder) than that of the other peptides.

Our functional and structural analyses therefore do not support the hypothesis of a greater instability for I-A^{g7}. First, our recombinant I-A^{g7} molecules do not exhibit a tendency to dissociate into monomers or to bind peptide to any lesser extent than I-A^d. Second, the crystal structure of I-A^{g7} is remarkably similar to that of other class II molecules, particularly I-A^d (*15*) and I-A^k (*24*). The peptide promiscuity of I-A^{g7} (and I-A^d) arises from a structural motif that is skewed toward selection of small alternating residues, be they hydrophobic or hydrophilic; this motif is commonly found in globular proteins. The motif's low stringency is further accentuated by a redundant P1 pocket (*35*, *36*) and, for I-A^{g7}, by a P9 pocket with broader specificity. Promiscuous binding by a class II MHC, like I-A^{g7}, can be a double-edged sword because it potentially allows the host to respond more efficiently to antigen challenge, and yet simultaneously increases the susceptibility toward developing an autoimmune response. The actual response will depend, to a large extent, on the host's genetic background; this is clearly seen for the NOD and the Biozzi (H-2^{dq1}) AB/H mouse (*37*), which both express only the class II MHC I-A^{g7}. NOD mice develop IDDM, whereas Biozzi mice develop high responses to all T cell–dependent antigens (*38*).

Structural differences between I-A^{g7} and the non–IDDM-associated I-A alleles I-A^d and I-A^k center around the β_1 α-helix and the P9 pocket. The P9 pocket is probably directly linked to the biology and pathology of I-A^{g7} because it affects peptide reper-

Table 1. Data collection and refinement statistics. For crystallization, acidic and basic leucine zippers were removed from I-A^{g7} by thrombin digestion, and the residual COOH-terminal spacer sequences were digested with carboxypeptidase B. Covalent I-A^{g7}–peptide complexes of GAD$_{207\text{-}220}$ and GAD$_{221\text{-}235}$ were concentrated to 10 mg ml^{-1} in 20 mM Hepes, 25 mM NaCl (pH 7.5) and screened for crystallization. Small crystals were obtained for I-A^{g7}–GAD$_{207\text{-}220}$ and enlarged by streak seeding (*42*). Crystals were then grown in 16 to 18% polyethylene glycol 4000, 0.2 M LiCl (pH 6.6), 1% 2-methyl-2,4-pentanediol and flash-cooled to 96 K with glycerol as a cryoprotectant (through a sequential soak in 1, 5, 10, and 15% glycerol). A single crystal was used to collect data at beamline 7-1 of the SSRL. Data were integrated in space group $C222_1$ (a = 95.1 Å, b = 110.1 Å, c = 96.1 Å) with DENZO (version 1.9.1) and reduced with SCALEPACK [version 1.9.0 (*43*)]. Crystal mosaicity was refined in batches and ranged from 1.0 to 1.3°. A single I-A^{g7} was assumed to be present in the asymmetric unit based on the calculated Matthew's coefficient [V_m ~ 2.9 Å^3/Dalton, ~57.0% solvent (*44*)]. Molecular replacement was carried out with CCP4's version of *AMoRE* (*45*, *46*) and the MHC class II search model I-A^k [PDB code 1iak (*24*)], in which the peptide, carbohydrate, and waters had been omitted. Clear rotation (one peak greater than 50% maximum peak height, resolution 8.0 to 3.5 Å, sphere radius 22.5 Å) and translation solutions (correct solution was 6.7σ above the next highest peak, resolution 8.0 to 3.5 Å) were found. After rigid body fitting within *AMoRE* (resolution 20.0 to 2.7 Å), the correlation coefficient was 68.7% and the R_{cryst} was 41.5%. Further rigid body refinement was carried out with CNS [version 0.9 (*47*)] by using three domains α_1/β_1, α_2, and β_2. The B_{value} for all atoms was then reset to 20 Å^2. Cross-validated σ_A-weighted $2F_o - F_c$ and $F_o - F_c$ electron density maps (*48*) were used throughout in order to rebuild and were viewed with the graphics program O (*49*). Density was observed for the peptide at this stage, but not refined until later. Because density for the helix region Gly β54 to Gln β64 was ambiguous, its occupancy was set to zero for the next refinement cycle (positional and torsion angle dynamics refinement, resolution 10.0 to 2.7 Å, with a starting temperature for the dynamics determined with the slow cool protocol of 4000 K). Density for the helix was noticeably improved and was gradually rebuilt over the next few cycles. R_{free} (*50*) (~10% of the reflections) was used from the outset to monitor the course of the refinement. Waters were picked toward the end of the refinement, with an $F_o - F_c$ map and a 3.5 to 4.0σ cutoff. Waters were rejected after refinement if they failed to appear in both $2F_o - F_c$ and $F_o - F_c$ maps, were not within hydrogen bonding distance of another protein atom or water molecule, or if their B_{value} exceeded 50 Å^2. All data from 40 to 2.6 Å were used in the last few refinement cycles, and an anisotropic B correction was applied along with a bulk solvent correction to give the final structure (*51*).

Data collection	
Resolution range (Å)	40.0–2.6
Unique reflections	15,754 (1545)*
Total number of reflections	66,107 (6531)
Completeness (%)	99.3 (99.6)
$\langle I/\sigma(I)\rangle$	15.7 (4.2)
R_{sym} (%)†	6.8 (35.3)
Refinement statistics	
Resolution range (Å)	40.0–2.6
Anisotropic correction (Å^2)	B_{11} = 8.0, B_{22} = −3.5, B_{33} = −4.5
R_{cryst}‡	0.210 (0.276)
R_{free}§	0.258 (0.344)
rmsd from ideality	
Bond length (Å)	0.006
Bond angle (°)	1.3
Dihedrals (°)	26.0
Impropers (°)	0.8
Average B_{value} (Å^2)	
I-A^{g7}	36.4
Peptide GAD$_{207-220}$	35.4
Waters	28.5
Ramachandran plot‖	
Favord (%)	90.2
Allowed (%)	9.2
Generous (%)	0.0
Disallowed (%)	0.6

*Data for the highest resolution shell (2.69 to 2.60 Å). †$R_{sym} = 100 \times [\Sigma_h \Sigma_i |I_i(h) - \langle I(h)\rangle| / \Sigma_h I(h)]$, where $I_i(h)$ is the ith measurement of the h reflection and $\langle I(h)\rangle$ is the average value of the reflection's intensity. ‡$R_{cryst} = \Sigma||F_o| - |F_c|| / \Sigma|F_o|$, where F_o and F_c are the observed and calculated structure factor amplitudes within the set of reflections used for refinement. §$R_{free} = \Sigma||F_o| - |F_c|| / \Sigma|F_o|$ calculated for a randomly selected set of structure factors (~10%) throughout the resolution range and not used in refinement. ‖The Ramachandran plot was generated with PROCHECK (*52*).

toire selection and, potentially, the nature of the interaction with the T cell receptor. The ability of I-A^{g7}, compared with other I-A alleles, to select for a novel subset of peptides has been demonstrated by a comparison of peptide binding to an I-A^{g7} where the β56 and β57 positions are changed back to the I-A^{d} sequence ($Pro^{\beta 56}$ and $Asp^{\beta 57}$, I-A^{g7}.PD); I-A^{g7} preferentially binds peptides with an acidic P9 residue, unlike its mutated counterpart I-A^{g7}.PD (*19*).

I-A^{g7} peptide complexes that have small nonacidic P9 residues, such as Gly/Ala, will leave an unfilled "oxyanion" hole. These complexes could conceivably bind a set of complementary T cell receptors that can contribute a negatively charged residue to the oxyanion cavity and provide additional stability. In support of this hypothesis, the recently determined I-A^{g7}- $GAD_{221-235}$ structure (*39*) has a Gly at the peptide P9 position; yet the P9 cavity is still occupied, but by a glutamate side chain from a symmetry-related molecule. Alternatively, other acidic residues present in the COOH-terminal extensions (P10 to P12) of the peptide itself could fill the oxyanion hole and hence lead to kinked conformations of the peptide that would appear very different to the T cell receptor.

Thus, the crystal structure of I-A^{g7} now provides a structural framework for unraveling the link between a class II molecule and a tissue-specific autoimmune process. The high number of peripheral autoreactive T cells present in NOD mice may be linked with poor central tolerance or may be the consequence of promiscuous or altered peptide binding of a class II MHC, in this case I-A^{g7}. In terms of therapeutic intervention at the level of MHC, the idea of "blocking peptides" has long been envisaged and tested exhaustively. Previous failures have probably arisen from their short half-lives, low bioavailability, and low specific binding. The crystal structure of I-A^{g7} should aid in the future design of novel high-affinity ligands for I-A^{g7}.

Table 2. Alignment of peptides with the canonical P1, P4, P6, and P9 pockets of the I-A^{g7} peptide-binding groove. Alignment of most of these peptides, within the I-A^{g7} peptide-binding groove, can be achieved with the optimal motif; the average affinity of these peptides should presumably be higher compared with peptides that bind using nonoptimal residues. Some of the peptides can adopt different registers, as has been observed for peptides that bind to I-A^{d} (*15*). Potential anchor residues at P1, P4, P6, and P9 are indicated in bold. Acidic P9 residues are colored red, whereas Gly/Ala or Ser at P9 are colored blue. Abbreviations for the amino acid residues are as follows: A, Ala; C, Cys; D, Asp; E, Glu; F, Phe; G, Gly; H, His; I, Ile; K, Lys; L, Leu; M, Met; N, Asn; P, Pro; Q, Gln; R, Arg; S, Ser; T, Thr; V, Val; W, Trp; and Y, Tyr.

	Peptide register																	
Peptide	-3	-2	-1	1	2	3	4	5	6	7	8	9	10	11	12	13	14	Ref.
$GAD65_{105-119}$*†‡			R	**P**	T	L	**A**	F	**L**	Q	D	**V**	M	N	I	L	L	
$GAD65_{207-220}$†§		Y	E	**I**	A	P	**V**	F	**V**	L	L	**E**	Y	V	T			(*19, 20*)
$GAD65_{221-235}$‖	L	K	K	**M**	R	E	**I**	I	**G**	W	P	**G**	G	S	G			(*19, 20*)
	K	M	R	**E**	I	I	**G**	W	**P**	G	G	**S**	G					
$GAD65_{286-300}$	K	K	G	**A**	A	A	**L**	G	**I**	G	T	**D**	S	V	I			(*19, 20*)
			K	**K**	G	A	**A**	A	**L**	G	I	**G**	T	D	S	V	I	
$GAD65_{401-415}$	P	L	Q	**C**	S	A	**L**	L	**V**	R	E	**E**	G	L	M			(*19*)
		P	L	**Q**	C	S	**A**	L	**L**	V	R	**E**	E	G	L	M		
$GAD65_{509-528}$	P	P	S	**L**	R	T	**L**	E	**D**	N	E	**E**	R	M	S	R	L	(*34, 35*)
$GAD65_{524-543}$	S	R	L	**S**	K	V	**A**	P	**V**	I	K	**A**	R	M	M	E	Y	(*34*)
$GAD65_{561-575}$			I	**S**	N	P	**A**	A	**T**	H	Q	**D**	I	D	F	L	I	(*19*)
	I	S	N	**P**	A	A	**T**	H	**Q**	D	I	**D**	F	L	I			
$OVA_{323-339}$¶	R	G	I	**S**	Q	A	**V**	H	**A**	A	H	**A**	E	I	N	E	A	(*53*)
	A	V	H	**A**	A	H	**A**	E	**I**	N	E	**A**	G	R				
Insulin B_{9-23}	S	H	L	**V**	E	A	**L**	Y	**L**	V	C	**G**	E	R	G			(*31, 54*)
λ REP_{12-26}#	L	E	D	**A**	R	R	**L**	K	**A**	I	Y	**E**	K	K	K			(*53*)
$Transferrin_{55-68}$	H	N	Y	**V**	T	A	**I**	R	**N**	Q	Q	**E**	G					(*8, 31, 35*)
hnRNP $A2_{51-66}$		V	V	**M**	R	D	**P**	A	**S**	K	R	**S**	R	G	F	G	F	(*8*)
$MSA_{560-574}$	K	A	T	**A**	E	Q	**L**	K	**T**	V	M	**D**	D					(*8, 31*)
ROI†,**	V	H	A	**A**	H	A	**V**	H	**A**	A	H	**A**	V	H	A			
Human $HSP60_{441-460}$			G	**C**	A	L	**L**	R	**C**	I	P	**A**	L	D	S	L	T	(*31, 55*)
		P	A	**L**	D	S	**L**	T	**P**	A	N	**E**	D					
	P	A	L	**D**	S	L	**T**	P	**A**	N	E	**D**						
$CLIP_{86-100}$	V	S	Q	**M**	R	M	**A**	T	**P**	L	L	**M**	R	P				(*31, 35*)
$Eα_{52-68}$	E	A	Q	**G**	A	L	**A**	N	**I**	A	V	**D**	K					(*8, 56*)
			E	**A**	Q	G	**A**	L	**A**	N	I	**A**	V	D	K			
HEL_{9-27}¶	A	M	K	**R**	H	G	**L**	D	**N**	Y	R	**G**	Y	S	L	G	N	(*40, 57*)
PLP_{56-70}		D	Y	**E**	Y	L	**I**	N	**V**	I	H	**A**	F	Q	Y	V		(*58*)

*All sequences are murine based, unless specified otherwise. †Own observations. ‡This peptide cannot be clearly aligned into the I-A^{g7} peptide groove with the aforementioned motif. The current alignment, although favorable for the pockets P1, P4, and P6, places a valine in the P9 pocket. Shifting this alignment by one residue to the right would place an Asp into the P9 pocket; however, this register would result in a Phe occupying the P6 pocket. §Sequence length is an average representation. Refer to references for specific details. ‖Only residues within the designated register are shown. ¶Chicken. #λ REP, bacteriophage λ repressor; hnRNP, heterogeneous nuclear ribonuclear particles; MSA, murine serum albumin; HSP, heat shock protein: PLP, proteolipid protein. **Synthetic peptide.

References and Notes

1. T. J. Vyse and J. A. Todd, *Cell* **85**, 311 (1996).
2. H. Acha-Orbea and H. O. McDevitt, *Proc. Natl. Acad. Sci. U.S.A.* **84**, 2435 (1987).
3. J. A. Todd, J. I. Bell, H. O. McDevitt, *Nature* **329**, 599 (1987).
4. S. M. Singer, R. Tisch, X. D. Yang, H. O. McDevitt, *Proc. Natl. Acad. Sci. U.S.A.* **90**, 9566 (1993).
5. T. Lund *et al.*, *Nature* **345**, 727 (1990).
6. R. Quartey-Papafio *et al.*, *J. Immunol.* **154**, 5567 (1995).
7. H. G. Rammensee, T. Friede, S. Stevanoviic, *Immunogenetics* **41**, 178 (1995).
8. E. P. Reich *et al.*, *J. Immunol.* **152**, 2279 (1994).
9. W. M. Ridgway and C. G. Fathman, *Curr. Opin. Immunol.* **11**, 638 (1999).
10. E. Carrasco-Marin, J. Shimizu, O. Kanagawa, E. R. Unanue, *J. Immunol.* **156**, 450 (1996).
11. R. Tisch and H. McDevitt, *Cell* **85**, 291 (1996).
12. C. A. Scott, K. C. Garcia, F. R. Carbone, I. A. Wilson, L. Teyton, *J. Exp. Med.* **183**, 2087 (1996).
13. H. Kozono, J. White, J. Clements, P. Marrack, J. Kappler, *Nature* **369**, 151 (1994).
14. T. Stratmann *et al.*, in preparation.
15. C. A. Scott, P. A. Peterson, L. Teyton, I. A. Wilson, *Immunity* **8**, 319 (1998).
16. Peptides were displayed as an NH_2-terminal fusion to the gene VIII product of M13 (*14*).
17. Competition assay to MHC class II molecules: A modified competition assay (enzyme-linked immunosorbent assay) (*40*) was used to determine binding of peptides to I-A^{g7} and I-A^{d} with biotinylated I-A^{g7}/I-A^{d}-specific ROI peptide and unlabeled test peptides. Briefly, a 96-well microtiter plate (Maxisorb, Nunc) was coated with the I-A^{g7}– and I-A^{d}–specific monoclonal antibody M5.114 [American Type Culture Collection, Manassas, VA; 100 μl/well, diluted in 50 mM $NaCO_3$ (pH 9.6) to a final concentration of 5 μg/ml] overnight at 4°C and washed five times with phosphate-buffered saline (PBS) containing 0.05% Tween-20. The plate was blocked with 200 μl of PBS containing 5% bovine serum albumin overnight at 37°C and washed as before. In a second plate, 200 ng of I-A^{g7} or I-A^{d} were incubated in 100 μl of binding buffer [6.7 mM citric phosphate (pH 10.4), 0.15 M NaCl, 2% NP-40, 2 mM EDTA] containing 0.5 to 1 μM biotinylated ROI peptide with test peptide (serially diluted 10-fold at six concentrations, 0.0005 to 50 μM) at 37°C overnight. The solutions were transferred to the antibody-coated plate and incubated for 4 hours at room temperature. The plates were washed 10 times with PBS containing 0.05% Tween-20 over a period of 1 hour, and washed five additional times with PBS over 30 min. The plate was incubated with PBS (100 μl/well) containing streptavidin-conjugated alkaline phosphatase (0.7 μg/ml) for 1 hour at room temperature and washed as before. Retained peptides were colorimetrically detected with ρ-nitrophosphate at 4°C overnight. Absorbance at $λ_{405nm}$ was determined with a 96-well plate reader (vmax kinetic microplate reader, Molecular Devices). Test peptides used in this study were pAla (AAAAAAAAAAA), pAla A^{10}→E (AAAAAAAAAEA), ROI (VHAAHAVHAAHAVHA), and MM 67 to 79 (CTVLTALGTILKK).
18. J. W. Yoon *et al.*, *Science* **284**, 1183 (1999).
19. C. C. Chao, H. K. Sytwu, E. L. Chen, J. Toma, H. O. McDevitt, *Proc. Natl. Acad. Sci. U.S.A.* **96**, 9299 (1999).
20. C. C. Chao and H. O. McDevitt, *Immunogenetics* **46**, 29 (1997).
21. Supplemental Web material is available at *Science* Online at www.sciencemag.org/feature/data/1049210.shl.
22. Superimposition, with ProFit (A.C.R. Martin, SciTech Software, 1996), of the MHC class II structures was done with residues in the β-sheet floor of the pep-

tide-binding groove. The specific residues were α18 to α26, α29 to α34, β24 to β32, and β37 to β42.
23. The crystal structures of I-A^d (*15*) complexed with peptides $OVA_{323-339}$ [Protein Data Bank (PDB) code 1IAO] or $HA_{126-138}$ (PDB code 2IAD) were each superimposed onto I-A^{g7} (*22*); both gave the same rmsd value to two significant figures.
24. D. H. Fremont *et al.*, *Immunity* **8**, 305 (1998).
25. This displacement actually encompasses $Ala^{\beta49}$ to $Ala^{\beta58}$, which contribute to part of the S4 β-strand, a connecting loop segment, and the start of the H1 α-helix. Maximum rms deviations between I-A^{g7} and I-A^d within this region are around residues β55 to β57. The C_α-C_α distances between the equivalent β55 to β57 residues in I-A^{g7} and I-A^d-$HA_{126-138}$ are 1.29, 1.76, and 1.19 Å, respectively.
26. $Tyr^{\beta61}$ is positioned near the end of the H1 α-helical segment, and its side chain forms part of the wall of the peptide-binding groove. Although the $Tyr^{\beta61}$ side chain of I-A^{g7} overlaps spatially with the corresponding residue $Trp^{\beta61}$ in I-A^d and I-A^k, differences (70° to 79°) in the torsion angle χ_2 resulted in the planes of the aromatic side chains being almost perpendicular to each other (Fig. 2C). Accommodation of the increased volume resulting from the side chain of $Tyr^{\beta61}$, parallel to the α helix of the domain, was achieved by displacement of the region $Ala^{\beta49}$ to $Ala^{\beta58}$. $His^{\beta9}$ in the S1 β-strand forms part of the floor of the peptide groove, and its side chain in I-A^{g7} only subtly perturbs the surrounding region when compared with I-A^d. However, movement of the I-A^{g7} $Tyr^{\beta37}$ side chain (by ~15° around χ_1), relative to I-A^d, allowed for the larger side chain of $His^{\beta9}$. A domino effect was seen in I-A^{g7} because movement of the $Tyr^{\beta37}$ side chain had itself to be accommodated. Displacement of the region $Leu^{\beta53}$ to $Ser^{\beta57}$ outward might, therefore, be due in part to the polymorphic residue $His^{\beta9}$.
27. E. A. Nalefski, K. T. Shaw, A. Rao, *J. Biol. Chem.* **270**, 22351 (1995).
28. A plot of the average B_{value} for each residue of the peptide showed minimal relative mobility. Minima occurred near the center of the peptide (P4 to P6), whereas maxima occurred at the COOH-terminus. These differences were completely consistent with those observed in I-A^d and I-A^k and were therefore not significant.
29. First, residue $Asn^{\alpha69}$ does not form a bidentate hydrogen bond with P7, as seen in most class II structures; instead, the P7 carbonyl oxygen hydrogen bonds to the side-chain hydroxyl of $Tyr^{\beta61}$. Also, the P8 carbonyl oxygen no longer hydrogen bonds with residue β61 owing to the absence of Trp at this position, but forms a substitute hydrogen bond with the hydroxyl of polymorphic residue $Tyr^{\beta66}$. This polymorphic position corresponds to the site of a two-residue deletion between the helical segments H1 and H2a, when compared with I-A^d, and leads to a rearrangement of the standard hydrogen bonding pattern with the P7 and P8 residues.
30. No hydrogen bonds with good geometry are made between these two residues.
31. D. H. Hausmann *et al.*, *J. Exp. Med.* **189**, 1723 (1999).
32. The $Pro^{\beta56}$ side chain creates an overhang (Fig. 2C) that buries a large part of the $Arg^{\alpha76}$ side chain. Substitution by $His^{\beta56}$ makes the side chain of $Arg^{\alpha76}$ much more accessible but does not directly destabilize the H1 segment of the β1 because its main-chain conformation and the adjacent residues are similar to that of I-A^d and I-A^k.
33. For HLA-DR1, position β56 is a putative contact for the coreceptor CD4 [J. Brogdon *et al.*, *J. Immunol.* **161**, 5472 (1998)]; the presence of $His^{\beta56}$, in I-A^{g7}, instead of the usual $Pro^{\beta56}$ could alter the type of signal transmitted to the $CD4^+$ T cell.
34. D. L. Kaufman *et al.*, *Nature* **366**, 69 (1993).
35. B. Reizis *et al.*, *Int. Immunol.* **9**, 43 (1997).
36. K. Bartnes *et al.*, *Int. Immunol.* **9**, 1185 (1997).
37. G. Y. Liu *et al.*, *Immunogenetics* **37**, 296 (1993).
38. C. Stiffel *et al.*, *Immunol. Lett.* **16**, 205 (1987).
39. A. L. Corper, L. Teyton, I. A. Wilson, unpublished data.
40. L. C. Harrison *et al.*, *J. Exp. Med.* **185**, 1013 (1997).
41. Biosym Technologies, San Diego, CA, USA.
42. E. A. Stura and I. A. Wilson, *J. Crystal Growth* **110**, 270 (1991).
43. Z. Otwinowski and W. Minor, *Methods Enzymol.* **276**, 307 (1997).
44. B. W. Matthews, *J. Mol. Biol.* **33**, 491 (1968).
45. CCP4, *Acta Crystallogr. D* **50**, 760 (1994).
46. J. Navaza, *Acta Crystallogr. A* **50**, 157 (1994).
47. A. T. Brünger *et al.*, *Acta Crystallogr. D* **54**, 905 (1998).
48. R. J. Read, *Methods Enzymol.* **277**, 110 (1997).
49. T. A. Jones, J. Y. Zou, S. W. Cowan, Kjeldgaard, *Acta Crystallogr. A* **47**, 110 (1991).
50. A. T. Brünger, *Nature* **355**, 472 (1992).
51. The final structure contains 3012 protein atoms, 76 solvent molecules, and no carbohydrate. The following residues were built for I-A^{g7}–$GAD_{207-220}$: α1B to α178, α1S to α2S, β5 to β104, β113 to β188, β1S and β207P to β220P. Density for the loop β105 to β112 was absent and was therefore not built. Side-chain density for the following residues was absent and was therefore truncated back to the C_β atom: $Asp^{\alpha18}$, $Lys^{\alpha40}$, $Lys^{\beta63}$, $Glu^{\beta85}$, $Asn^{\beta113}$, $His^{\beta166}$, $Tyr_{\beta207P}$, $Tyr_{\beta218P}$, and $Thr_{\beta220P}$. Residues α1S, α2S, and β1S are the remains of the spacer(s), whereas β207P to β220P is the tethered GAD peptide.
52. R. A. Laskowski *et al.*, *J. Appl. Crystallogr.* **26**, 283 (1993).
53. D. E. Smilek, C. B. Lock, H. O. McDevitt, *Immunol. Rev.* **118**, 37 (1990).
54. D. Daniel and D. R. Wegmann, *Proc. Natl. Acad. Sci. U.S.A.* **93**, 956 (1996).
55. D. Elias *et al.*, *Proc. Natl. Acad. Sci. U.S.A.* **88**, 3088 (1991).
56. E. Carrasco-Marin, O. Kanagawa, E. R. Unanue, *Proc. Natl. Acad. Sci. U.S.A.* **96**, 8621 (1999).
57. U. Hurtenbach *et al.*, *J. Exp. Med.* **177**, 1499 (1993).
58. S. Amor *et al.*, *J. Immunol.* **150**, 5666 (1993).
59. NH_2-terminal Edmann degradation of the β chain of I-A^{g7} was carried out in order to confirm the GAD_{207} sequence. The 19 residues that were sequenced (gsh-srgYEIAPVFVLLEYV) correspond to part of the signal peptide (lowercase) and the correct sequence for $GAD_{207-219}$.
60. T. S. Jardetzky *et al.*, *Nature* **368**, 711 (1994).
61. K. J. Smith *et al.*, *J. Exp. Med.* **188**, 1511 (1998).
62. A. Dessen *et al.*, *Immunity* **7**, 473 (1997).
63. I. K. McDonald and J. M. Thornton, *J. Mol. Biol.* **238**, 777 (1994).
64. Calculated within the Viewer module of Insight II (*41*). Extended VDW radii were used.
65. We thank the staff at SSRL beamline 7-1, and H. McDevitt, D. Fremont, H. Grey, M. Taussig, and D. Williams for helpful discussions. Special thanks to N. Sarvetnick for the GAD65 peptide library, to A. Lehuen and J. Fehling for providing the cDNAs for I-A^{g7} β and GAD65, and to R. Stanfield for data collection and analysis. Supported by NIH grants CA58896 (I.A.W.) and DK55037 (L.T.) and by a National Health and Medical Research Council of Australia. C. J. Martin Fellowship (V.A.). This is publication 13001-MB from the Scripps Research Institute. The coordinates and structure factors for I-A^{g7}–$GAD_{207-220}$ have been deposited without hold in the PDB (access code 1ES0) and are available immediately from wilson@scripps.edu

4 February 2000; accepted 28 March 2000

The Eye Injury of King Philip II and the Skeletal Evidence from the Royal Tomb II at Vergina

Antonis Bartsiokas

The Royal Tomb II was discovered in Vergina, Greece, in 1977. It contained a male skeleton and a rich array of grave goods. Evidence of trauma supposedly in the orbital bones of the skull has been thought to correspond to an eye injury that King Philip II is historically known to have suffered. However, reexamination of the orbital morphology showed no evidence of such pathology. Therefore, the skeleton does not belong to Philip II. New skeletal evidence shows that the skeleton belongs to King Philip III Arrhidaeus. In this case, the tomb may well contain some of the paraphernalia of Alexander the Great.

A tomb designated Royal Tomb II was discovered at Vergina by Andronicos in 1977 (*1*). It was divided into two chambers. The main chamber contained a marble sarcophagus inside of which a golden chest (or larnax) bearing the Macedonian star burst was discovered. The chest contained the almost complete cremated skeleton of a man. Within the antechamber, a similar sarcophagus and chest were discovered, containing the cremated skeleton of a woman. The richness of the grave goods was astonishing. Among them, two small ivory heads have been identified as those of King Philip II and Alexander the Great (*1*). There were also a gilded silver diadem, a gold-sheathed sceptre, an iron and gold cuirass, an iron helmet, and an elaborate ceremonial shield (*1*). Considerable interest has been focused on the identification of the male occupant of the tomb. Andronicos, on the basis of archaeological evidence that pointed to a date around 336 B.C., identified the tomb as that of King Philip II of Macedon (*1*), father of Alexander the Great. However, mounting archaeological evidence (*2*, *3*) that points to a date around 317 B.C. suggests that the tomb belongs to King Philip III Arrhidaeus, son of Philip II and half-brother of Alexander the Great. As a result, the anthropological evidence became crucial to test the archaeological hypotheses.

The aim here is to study the paleopathology of the male skeleton using macrophotography, because no close-up pictures of his injuries had ever been obtained to study the microstructure of the wounds. Macropho-

Anaximandrian Institute of Human Evolution, 6 Aeginis Street, GR-166 73 Voula, Greece. E-mail: anaxbart@otenet.gr